Dalton Transactions

ROYAL SOCIETY OF CHEMISTRY

PAPER

View Article Online
View Journal

Cite this: DOI: 10.1039/d6dt00262e

New insights into the photocatalytic properties of composites based on TiO_2 and single-walled carbon nanotubes

Adelina Udrescu,[a] Ion Smaranda,[a] Radu Cercel,[a] Andreea Androne,[a,b] Andreea Nila,[a] Elena Matei,[a] Ionel Mercioniu,[a] Stefano Bellucci[a] and Mihaela Baibarac *[a]

Composites based on TiO_2 and single-walled carbon nanotubes (SWCNTs), highly separated in semiconducting tubes (S-SWCNTs) and as a mixture of metallic and semiconducting tubes (M + S-SWCNTs), were obtained by the interaction in the solid state. This interaction induces a change in the size of TiO_2 particles from 23.67 nm to 28.2 and 150 nm, respectively, accompanied by an increase in the disorder state of the graphitic lattice of SWCNTs. We demonstrate by UV-VIS spectroscopy that the best performance in terms of rhodamine 6G (Rh6G) photodegradation is obtained in the case of the TiO_2/S-SWCNT composite. The highest values of the Rh6G photodegradation efficiency were equal to 92% for an S-SWCNT concentration in the photocatalyst mass of 10 wt% and 94% for a 0.1 mM Rh6G solution with a pH equal to 1. We demonstrate that an important role is played by the $O_2^{\bullet-}$ and $^{\bullet}OH$ species in the photodegradation mechanism of Rh6G. This study contributes to a better understanding of the role of metallic and semiconducting carbon nanotubes in the photocatalysis field, highlighting that composites based on semiconducting SWCNTs and semiconducting metallic oxides are those that contribute essentially to the removal of dyes by exposure to the light emitted by a halogen lamp.

Received 31st January 2026,
Accepted 17th June 2026

DOI: 10.1039/d6dt00262e

rsc.li/dalton

1. Introduction

Since 2005, special attention has been paid to composites based on TiO_2 and carbon nanotubes (CNTs) in the field of photocatalysis.[1] Several review articles were published regarding the enhancement of the photocatalytic properties of TiO_2 in the presence of carbon-containing materials[2] for the removal of organic pollutants.[3] The interest in these composites was a consequence of the absorption of TiO_2 in the UV range, presenting a limitation of the fast electron–hole recombination, disadvantages compensated by CNTs, which present electrical, structural, and absorption properties that allow the improvement of the properties of TiO_2.[4] The main synthesis methods developed for the TiO_2/CNT composites were: (i) the sol–gel method, which allows a relatively uniform dispersion of TiO_2 nanoparticles on the surface of CNTs;[5] (ii) hydrothermal synthesis, which leads to larger particles, exhibiting lower photocatalytic activity;[6] (iii) the chemical vapor deposition (CVD), the method reported as allowing better control of the interface of the two constituents, the resulting composite with high photocatalytic performances;[7] (iv) solvothermal way, which allows expansion of absorption in VIS range;[8] (v) multilayers of TiO_2 and CNTs, which reduce contact resistance and increase photoelectrochemical efficiency;[9] and (vi) *in situ* growth of TiO_2 in the presence of CNTs by sol-reflux method, leading to the heterojunctions of the type CNT/TiO_2 that facilitate the transfer of free electrons from TiO_2 to CNTs.[10] Taking into account this progress, in this work, for the preparation of the composites based on TiO_2 and CNTs, the interaction in the solid state will be used. A detailed understanding of the interactions that take place during the preparation of composites using the solid-state interaction starting from TiO_2, a mixture of metallic (33%) and semiconducting (66%) single-walled carbon nanotubes (M + S-SWCNTs), as well as SWCNTs highly separated into semiconducting tubes (S-SWCNTs, 99%), respectively, will be presented through correlated studies of high-resolution transmission microscopy (HRTEM), scanning electron microscopy (SEM), X-ray diffraction (XRD), Raman scattering, and, finally, UV-VIS spectroscopy.

The main pollutants removed with photocatalysts based on TiO_2 nanoparticles and CNTs were: (i) pharmaceutical compounds such as carbamazepine, diclofenac, sulfamethoxazole,[11] tetracycline,[12] *etc.*, (ii) dyes, such as methylene Blue (MB),[13] rhodamine B (RhB),[14] methyl orange (MO),[15] *etc.* and

[a]*National Institute of Materials Physics, Laboratory of Optical Processes in Nanostructured Materials, Atomistilor street 405A, Magurele, Romania. E-mail: barac@infim.ro*
[b]*University of Bucharest, Faculty of Physics, Atomistilor Street 405, Magurele, Romania*

(iii) insecticides, such as carbofuran.[13] In the present work, our attention will be focused on rhodamine 6G (Rh6G). To obtain the highest possible photodegradation efficiency of organic pollutants, the optimization of photocatalysts involved identifying: (i) an optimal TiO_2/CNT weight ratio, reported to be between 1.5 and 20 wt%;[16–18] (ii) the optimal calcination temperature, reported to be between 300–1100 °C;[19] (iii) the influence of the type of CNTs in the TiO_2/CNT composites mass, when the composites based on TiO_2 and SWCNT were reported to show a photodegradation efficiency superior to those corresponding to composites based on TiO_2 and CNTs of the type double-wall carbon nanotubes or multi-wall carbon nanotubes;[16] and (iv) the influence of the functional groups onto SWCNT surface of the type carboxyl (SWCNT-COOH) in the mass of the TiO_2/SWCNT-COOH composite, that induce the photodegradation efficiency superior to those of the TiO_2/SWCNT composite.[20] Although important progress has been reported in the case of TiO_2/CNT composites, there is little information about the effect of the outer wall type of CNTs on the photocatalytic process. As is well known, regardless of the synthesis method of CNTs, in the case of: (a) SWCNTs, results a mixture of metallic (33%) and semiconducting (66%) tubes (M + S-SWNTs),[21] (b) double-wall carbon nanotubes (DWNTs), are obtained a mixture of CNTs with the inner and outer tubes, of the type metallic@semiconducting (M@S) tubes, metallic@metallic (M@M) tubes, semiconducting@semiconducting (S@S) tubes and semiconducting@metallic (S@M) tubes,[22] and (c) multi-walled carbon nanotubes (MWNTs), are reported mixtures having outer tubes both of the type metallic and semiconductor.[23] The development of techniques for separating semiconductor tubes from metallic ones in SWCNT samples has opened new opportunities in understanding various optical processes.[24] This has allowed the preparation of SWCNTs highly separated into semiconducting tubes (S-SWCNTs, 99%) and metallic tubes (98%, M-SWCNTs).[25] In this work, the influence of S-SWCNTs and M-SWCNTs in the TiO_2/S-SWCNT and TiO_2/M-SWCNT composites in comparison with the TiO_2/M + S-SWCNT composite in the field of photocatalysis will be reported. Thus, we will highlight the importance of S-SWCNTs in optimizing the photodegradation processes of the dye Rh6G. Our results will prove that the photodegradation efficiency of Rh6G is higher in the case of TiO_2/S-SWCNT photocatalyst compared to that of the TiO_2/M + S-SWCNT and TiO_2/M-SWCNT photocatalysts.

2. Experimental section

Compounds TiO_2, Rh6G, HCl 36%, NaOH, isopropyl alcohol (IPA), and *tert*-butyl alcohol (TBA) were purchased from Sigma-Aldrich, while M + S-SWCNTs, M-SWCNTs, and S-SWCNTs were purchased from NanoIntegris.

The following composites TiO_2/M + S-SWCNT, and TiO_2/S-SWCNT, having a concentration of carbon nanotubes equal to 1 wt%, 5 wt%, and 10 wt%, were prepared by the solid-state interaction of the two constituents, *i.e.,* TiO_2 and CNTs, by manual grinding of the two constituents in an agate mortar and pestle for 20 min. To illustrate the role of M-SWCNT in the photocatalytic process, composites based on TiO_2 and M-SWCNTs with a concentration of CNTs of 1 wt.% were also prepared.

For photocatalytic studies, colloidal solutions were prepared by adding each composite to 20 mL of Rh6G 0.1 mM aqueous solution, which was magnetically stirred for 20 min at 25 °C in the dark to reach the adsorption–desorption equilibrium. After verifying by UV-VIS spectroscopy that the adsorption–desorption equilibrium of the pollutant on the photocatalyst surface had been reached, the colloidal solutions were exposed to an irradiation source consisting of a 300 W OSRAM halogen lamp (OSRAM GmbH, Germany), which provides a continuous broadband emission in the visible range (≈400–700 nm) and also emits infrared radiation. The irradiation time was 480 min.

The reaction temperature was continuously monitored using a K-type thermocouple connected to the digital display of the magnetic stirrer, with the probe immersed directly in the reaction mixture. Throughout the photocatalytic experiments, the temperature remained stable, with fluctuations within ±0.5 °C.

Dye degradation was monitored *in situ* by recording UV–Vis spectra directly in the quartz cuvette, without withdrawing successive aliquots; therefore, the total suspension volume remained constant during the reaction, eliminating any risk of overestimating photocatalytic activity due to gradual volume loss.

To prevent evaporation during irradiation, the quartz cell was fitted with a tight lid and positioned 12 cm away from the halogen lamp, which minimized thermal exposure of the solution.

HRTEM images and selected area electron diffraction (SAED) of the TiO_2, TiO_2/M + S-SWCNT, TiO_2/M-SWCNT, and TiO_2/S-SWCNT samples were recorded with a Jeol ARM 200 F microscope.

SEM images of the TiO_2/M + S-SWCNT, and TiO_2/S-SWCNT composites were recorded with a Zeiss Gemini 500 scanning electron microscope.

XRD diagrams of the TiO_2/M + S-SWCNT, and TiO_2/S-SWCNT composites were recorded with Bruker's D8 Advance X-ray diffractometer.

Raman spectra of TiO_2, M + S-SWNTs, S-SWNTs, and their composites of the type TiO_2/M + S-SWCNTs, and TiO_2/S-SWCNTs were recorded with a FTRaman spectrophotometer, MultiRam model, from Bruker.

Raman spectra of M-SWNTs and the TiO_2/M-SWCNTs composite were recorded with a Raman spectrophotometer, T64000 model, from Horiba Jobin Yvon, endowed with a Cobolt solid laser, which allows the recording of the spectra at the excitation wavelength of 633 nm.

UV-VIS spectra of the aqueous solutions of Rh6G in the presence of the TiO_2/M + S-SWCNT, TiO_2/M-SWCNT and TiO_2/S-SWCNT composites were recorded with a PerkinElmer Lambda 950 UV–VIS–NIR spectrophotometer.

Photoluminescence (PL) spectra of TiO_2, and their composites of the type TiO_2/M + S-SWCNTs, TiO_2/M-SWCNTs and TiO_2/S-SWCNTs were recorded with a Fluorolog spectrophotometer, FL-3.2.2 model, from Horiba-Jobin Yvon, at the excitation wavelength of 360 nm in the right-angle geometry.

Electrochemical impedance spectroscopy (EIS) measurements were performed in a three-electrode configuration using the TiO_2 and TiO_2/S-SWCNT, TiO_2/M-SWCNT, and TiO_2/M + S-SWCNT films deposited on ITO as working electrodes, a Pt wire as counter electrode, and an Ag/AgCl reference electrode in an aqueous H_2SO_4 0.05 M. The working electrodes were prepared as follows: 2 mg of each photocatalyst in powder form were dispersed in 1 ml of ethanol, followed by the addition of 10 μl of Nafion 0.5 wt%. The mixture was ultrasonicated for 10 min to obtain a homogeneous dispersion. Subsequently, 10 μl of this resulting ink was drop-cast onto ITO substrates and dried at 80 °C, yielding a uniform, adherent, and electrochemically active film. The impedance spectra were recorded in the frequency range 10 Hz–100 kHz with an AC amplitude of 10 mV.

3. Results and discussion

3.1 Optical, structural, and vibrational properties of composites based on TiO_2 and SWCNTs

Morphological information regarding TiO_2 nanoparticles and their composites with CNTs are presented in Figs. 1 and 2 by SEM, HRTEM, and SAED. In this context, Fig. 1 highlights the presence of both S-SWCNTs and M + S-SWCNTs and irregular platelets in the composites TiO_2/S-SWCNT and TiO_2/M + S-SWCNT. In the case of the TiO_2/S-SWCNT composite (Fig. 1a), one observes more compact particles and a smoother surface, while in the case of the TiO_2/M + S-SWCNT composite (Fig. 1b), the presence of the M + S-SWCNT induces a granular morphology with an interconnection of TiO_2 particles through M + S-SWCNTs.

Fig. 2 shows HRTEM images and SAED of the samples TiO_2, TiO_2/S-SWCNT, TiO_2/M-SWCNT, and TiO_2/M + S-SWCNT. According to Fig. 2, one observes that: (i) TiO_2 nanoparticles with an anatase crystalline phase have average dimensions equal to ≈23.67 nm; (ii) TiO_2/S-SWCNT composites contain particles with platelet morphology of various shapes with average dimensions of ≈28.2 nm; (iii) TiO_2/M + S-SWCNT composites illustrate the presence of platelet-like particles of various shapes with average dimensions of ≈150 nm. The increase in size indicates a coalescence of TiO_2 assisted by the SWCNT interface.

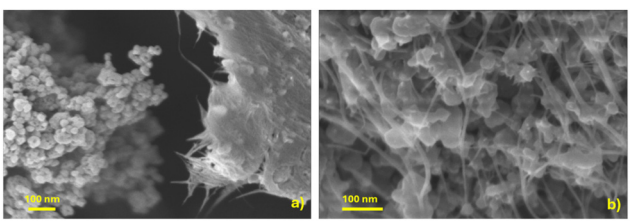

Fig. 1 SEM images of the composites of the type: (a) TiO_2/S-SWCNT, and (b) TiO_2/M + S-SWCNT, having a concentration of carbon nanotubes in each sample equal to 1 wt.%.

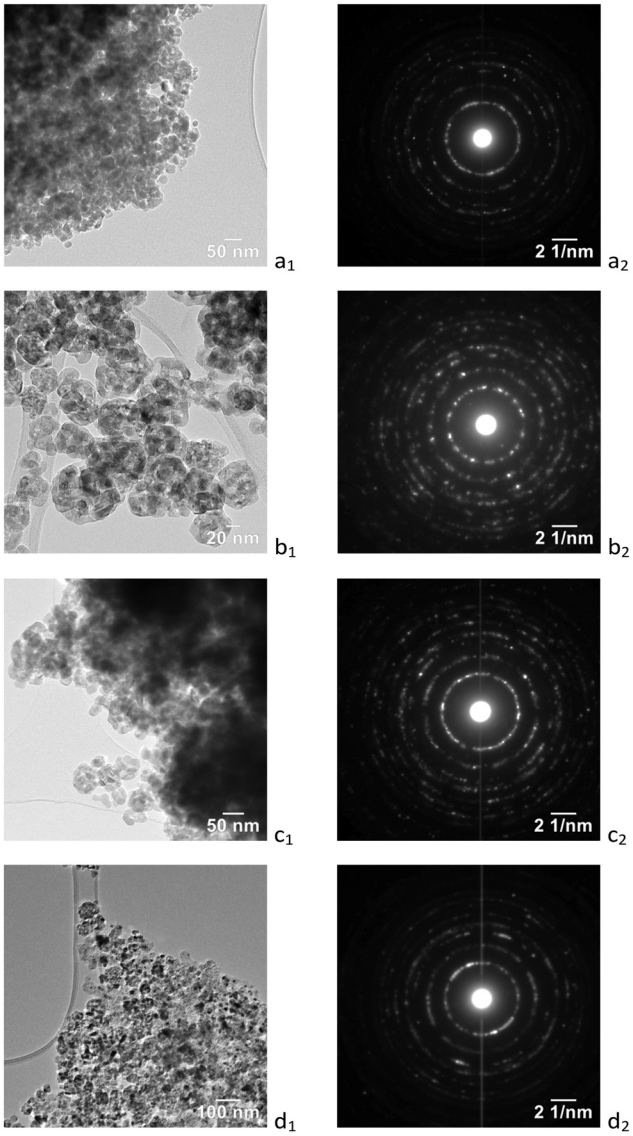

Fig. 2 HRTEM images and SAED of TiO_2 (a_1, a_2), and their composites of the type TiO_2/S-SWCNT (b_1, b_2), TiO_2/M-SWCNT (c_1, c_2), and TiO_2/M + S-SWCNT (d_1, d_2), with a concentration of carbon nanotubes in each sample equal to 1 wt.%.

The coalescence process of TiO_2 particles is seen to occur predominantly in the presence of semiconducting SWCNTs. An explanation for this behavior must take into account the electron transfer between the two constituents, the generation of a depletion zone in TiO_2, and the local electric field at the interface, which allows oxygen vacancies to migrate, defects to redistribute, and the energy of the TiO_2 grain boundaries to decrease, thus favoring the coalescence of TiO_2 crystallites.

Fig. 3 shows XRD diagrams of TiO_2, TiO_2/S-SWCNT, and TiO_2/M + S-SWCNT. All XRD diagrams are characterized by

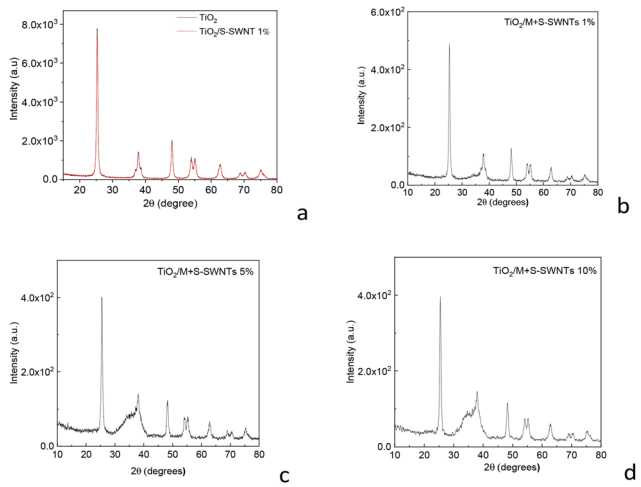

Fig. 3 XRD diagrams of TiO_2 (black curve, a) and their composites of the type TiO_2/S-SWCNT (red curve, a), when the concentration of S-SWCNT in the composite mass is 1 wt.%. XRD diagrams of the TiO_2/M + S-SWCNT composites, when the concentration of M + S-SWCNT in the composite mass is equal to 1 wt.% (b), 5 wt.% (c) and 10 wt.%.

peaks at 2θ equal to 25.3°, 37.8°, 48.2°, 54.1°, 55.3°, 62.8°, 70.4°, and 75.2° assigned to the crystalline planes of TiO_2 in anatase state (101), (004), (200), (105), (211), (213), (220), and (215), respectively [PDF 00-064-0863]. Using the Scherrer equation, the average crystallite size was calculated to be, in the case of: (a) TiO_2, 15.51 nm, (b) TiO_2/S-SWCNT, with 1 wt% SWCNT, 15.52 nm; (c) TiO_2/M + S-SWCNT, with 1 wt% M + S-SWCNT, 14.44 nm, (d) TiO_2/M + S-SWCNT, with 5 wt% M + S-SWCNT, 13.96 nm, and (e) TiO_2/M + S-SWCNT, with 10 wt% M + S-SWCNT, 13.74 nm. These results indicate that M-SWCNTs alone do not significantly influence the TiO_2 crystallite size, while mixed M + S-SWCNTs induce a progressive reduction. This suggests a stronger interfacial interaction and greater deformation/defect formation when both M-SWCNTs and S-SWCNTs are present. This behavior can be attributed to the heterogeneous electronic structure of M + S-SWCNTs. While S-SWCNTs and M-SWCNTs interact weakly and uniformly with the TiO_2 surface individually – resulting in crystallite sizes comparable to pristine TiO_2, M + S-SWCNTs produce a non-uniform interfacial electronic environment, which enhances local charge transfer, generating interfacial tension with the formation of defects in the TiO_2 lattice, thus inhibiting crystallite growth. The systematic decrease in crystallite size as the concentration of M + S-SWCNTs in the bulk composite occurs supports this mechanism, indicating that the M + S-SWCNT interaction is responsible for the reduction of TiO_2 crystallite size. The decrease in the crystallite size of TiO_2 in the presence of SWCNT is seen to be contradictory to the results reported by HRTEM. In our opinion, the increase in the size of the particles reported by HRTEM is the result of the agglomeration around the SWCNT network, while the decrease in the crystallite size originates from the strain and defect formation induced by metallic nanotubes from M + S-SWCNTs. The increase in the concentration of carbon nanotubes in the TiO_2/M + S-SWCNT composites leads in the XRD diagrams presented in Fig. 3c and d to a change in the shape of the maximum in the 2θ range 30°–40°, with the appearance of a new peak at 340. At first sight, this peak should be assigned to the crystalline plane (110) [PDF 01-070-2556]. However, taking into account that this peak is very large, we are tempted to attribute the interfacial deformations and defect-rich regions. Compared to the TiO_2/S-SWCNT composite, in the case of the TiO_2/M + S-SWCNT composite, the presence of metallic nanotubes leads to strong electronic shielding, which inhibits coherent charge transfer and defect migration, the locally distorted TiO_2 domains giving rise to diffuse scattering.

The same does not happen in the case of the TiO_2/S-SWCNT composite, in which the S-SWCNT facilitates defect reorganization and crystallite coalescence, the medium-range order characteristics being thus significantly diminished. The increase in the intensity of the peak at 34° in the case of the TiO_2/M + S-SWCNT composites with an S-SWCNT concentration of 5 and 10 wt.% can be explained by considering local structural changes of TiO_2, resulting in partial reduction of TiO_2 [26] and/or micro-deformation[27] that may occur during solid-state interaction.

Fig. 4 shows Raman spectra of TiO_2, S-SWCNTs, M + S-SWCNTs, and their composites. The black curve in Fig. 4a highlights, in the case of TiO_2, four lines that peaked at 146, 396, 518, and 639 cm^{-1}, assigned to the vibrational modes E_g, B_{1g}, A_{1g}, and E_g.[28] In the case of the Raman spectra of S-SWCNTs (blue curve in Fig. 4a), and M + S-SWCNTs (black curve in Fig. 4b) are observed: (a) in the low-frequencies, an intense Raman line at 162 and 164 cm^{-1}, respectively, assigned to the radial breathing mode (RBM), which is correlated with the diameter of the tubes through the equation: $\upsilon(cm^{-1}) = 248\ d^{-1}$ (nm),[23] indicating diameters equal to 1.53 and 1.51 nm, respectively; and (b) in the spectral range 1000–1700 cm^{-1}, an intense band at 1593 cm^{-1} assigned to the tangential mode (TM)[21] and a band of low intensity at 1265 and 1269 cm^{-1} attributed to the disorder state or defects from the graphitic lattice of SWNT.[21] Besides, a careful analysis of Fig. 4 indicates that the ratio between the intensities of the Raman lines peaked at: (a) 1265–1269 and 1596 cm^{-1} (I_D/I_{TM}) is equal to 0.079 in both cases; and (b) 162–164 and 1593 cm^{-1} (I_{RBM}/I_{TM}) is equal to 1.36 (black curve in Fig. 4a) and 0.76 (blue curve in Fig. 4b).

Fig. 4 highlights the following changes in the Raman spectra of the composites with 1 wt.% CNTs in the case of:

(a) the TiO_2/S-SWCNT composite, an up-shift of the Raman lines from 146, 162, 518 and 1265 cm^{-1} (red curve in Fig. 4a) to 147, 167, 514 and 1276 cm^{-1}, respectively (red curve in Fig. 4b), accompanied of a change of the ratios I_D/I_{TM} and I_{RBM}/I_{TM} to ~0.2 and ~0.35 (red curve in Fig. 4a); the up-shift of RBM was explained considering the mechanical interactions of the foreign type at the interface (compressive)[29] and the local perturbations of the Ti–O network due to electronic interface reasons (*e.g.* generation of Ti–O–C bonds),[30] and

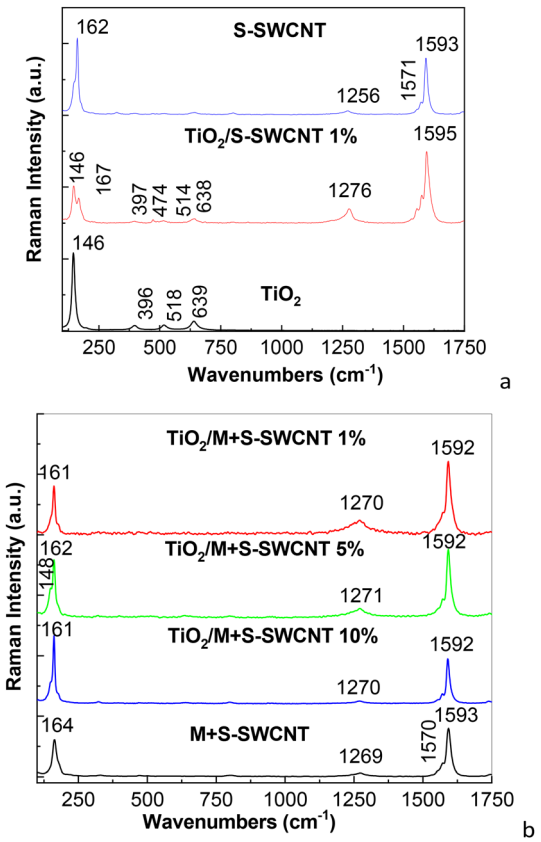

Fig. 4 Raman spectra of: (a) TiO_2 (black curve), S-SWCNT (blue curve), and TiO_2/S-SWCNT 1 wt.% (red curve), and (b) M + S-SWCNTs (black curve), TiO_2/M + S-SWCNT with a M + S-SWCNT concentration in composite mass equal to 10 wt.% (blue curve), 5 wt.% (green curve) and 1 wt. % (red curve).

(b) the TiO_2/M + S-SWCNT composite, a downshift of the Raman line from 164 to 161 cm^{-1}, accompanied by a change of the ratios I_D/I_{TM} and I_{RBM}/I_{TM} to ~0.2 and ~0.66 (red curve in Fig. 4b). The downshift of the RBM mode can be attributed to compressive mechanical stresses transmitted from the TiO_2 matrix to the M + S-SWCNTs. These stresses arise from interfacial interactions such as lattice mismatch, nanoparticle anchoring on defect sites, and local deformation of the nanotube walls. Similar strain-induced Raman shifts have been reported for TiO_2–CNT composites, regardless of the synthesis route, as demonstrated by Nadafan *et al.*[31] The increasing I_D/I_{TM} ratio value in the case of composites TiO_2/S-SWCNT and TiO_2/M + S-SWCNT in contrast with those reported in the case of S-SWCNTs and M + S-SWCNTs, indicates introducing defects or functional groups onto the SWCNT surface through mechanico-chemical interaction with TiO_2.[20] A similar behavior is reported in the Raman spectra recorded at 633 nm, the resonant wavelength for metallic carbon nanotubes (Fig. S1), in the case of Raman bands labeled as D and TM bands that have peaks at 1321–1318 and 1588–1590 cm^{-1}. In this case, a pronounced increase in the I_D/I_{TM} ratio is reported from 0.18 for M-SWCNT to 0.48 for the TiO_2/M-SWCNT composite. This substantial increase indicates a higher defect density in the carbon nanotubes after composite formation, probably associated with interfacial Ti–O–C bonds and partial disruption of the graphitic structure. The stronger perturbation observed in our case compared to the mild changes reported by Corio *et al.*[32] can be attributed to the different preparation route, *i.e.*, impregnation method, and to the higher sensitivity of metallic SWCNTs to mechano-chemical defect generation. The increase in the concentration of M + S-SWCNT in the TiO_2/M + S-SWCNT composite mass from 1 wt.% (red curve in Fig. 4b) to 5 wt.% (green curve in Fig. 4b) and 10 wt.% (blue curve in Fig. 4b) induce changes in the ratios I_D/I_{TM} and I_{RBM}/I_{TM} up to ~0.15 and ~0.85 (green curve in Fig. 4b) and ~0.07 and ~1.51 (blue curve in Fig. 4b). The decrease of the I_{RBM}/I_{TM} ratio in TiO_2/S-SWCNT and TiO_2/M + S-SWCNT composites indicates, once more, the presence of surface defects and interfacial charge transfer between TiO_2 and the nanotubes, as well as strain effects induced by TiO_2 nanoparticles on the RBM mode. By "surface defects" we refer to structural irregularities in the SWCNT lattice, such as pentagon–heptagon topological defects (Stone–Wales), vacancies, or oxygen-containing functional groups, which disrupt the ideal hexagonal sp^2 network and create active sites for TiO_2 anchoring. Although refs. 30 and 33 employ different synthesis routes, both demonstrate that TiO_2–CNT interfacial contact leads to defect formation, electronic coupling, and Raman intensity modifications, supporting the interpretation of our solid-state composites. In addition, ref. 34 reports that TiO_2 nanoparticles can induce mechanical strain on CNT walls, consistent with the RBM downshift observed in our samples.

To further correlate the structural features revealed by Raman spectroscopy with the electronic behavior of the materials, photoluminescence (PL) measurements were performed on TiO_2 and the TiO_2/SWCNT composites. Thus, Fig. S2 shows PL spectra of TiO_2 and the TiO_2/SWCNT composites recorded at the excitation wavelength of 360 nm. All samples exhibit an emission maximum at 2.82 eV, but with different intensities as follows. TiO_2 shows a PL intensity of 8.5×10^4 counts/sec, while the TiO_2/M + S-SWCNT and TiO_2/M-SWCNT composites display significantly lower values of 2.89×10^4 and 5.49×10^4 counts/sec, respectively. This decrease in the PL intensity indicates a PL quenching process, which involves a more efficient suppression of radiative electron–hole recombination in these two composites compared to pristine TiO_2. In contrast, the TiO_2/S-SWCNT composite exhibits a much higher PL intensity of 4.01×10^5 counts/sec, suggesting the presence of additional radiative pathways or defect-related emissive states introduced by S-SWCNT. Although the TiO_2/S-SWCNT composite exhibits a significantly higher PL intensity at 2.82 eV compared to the other samples, this behavior reflects the presence of additional radiative pathways or defect-related emissive states introduced by S-SWCNT rather than an increase in electron–hole recombination. The PL response therefore highlights differences in the electronic structure of the composites, but it does not directly predict photocatalytic efficiency. As discussed in the following section, the TiO_2/S-SWCNT composite displays the highest photocatalytic

performance, indicating that efficient non-radiative charge-transfer processes and ROS-generating pathways remain active despite the enhanced radiative emission observed in PL.

To further evaluate interfacial charge-transfer processes, EIS measurements were performed on TiO_2 and the TiO_2/SWCNT composites (Fig. S3). The Nyquist plots reveal a non-monotonic behavior of the charge-transfer resistance (R_{ct}), with semicircle diameters decreasing in the order TiO_2 > TiO_2/M + S-SWCNT > TiO_2/S-SWCNT, indicating more efficient charge transfer for the TiO_2/S-SWCNT and TiO_2/M + S-SWCNT composites. In contrast, the TiO_2/M-SWCNT sample exhibits a larger semicircle than pristine TiO_2, suggesting that M-SWCNTs form less favorable interfacial contacts and may introduce recombination pathways or Schottky-type barriers that impede electron injection. These observations correlate well with the PL results (Fig. S2). The high PL intensity of TiO_2/S-SWCNT reflects the presence of additional radiative or defect-related emissive states rather than inefficient charge separation, consistent with its low R_{ct}. Conversely, the partial PL quenching observed for TiO_2/M-SWCNT does not correspond to improved charge transfer, in agreement with its increased R_{ct}. Overall, the combined PL and EIS analyses indicate that the semiconducting SWCNT fraction plays the dominant role in facilitating interfacial charge separation and transport in these composites.

With all this information in mind, the performance of these photocatalysts will be highlighted in the next section.

3.2 Photocatalytic properties of composites based on TiO_2 and SWCNTs

Fig. 5 shows the UV-VIS spectra of the aqueous solution of Rh6G 0.5 mM in the presence of 0.2 mg ml^{-1} photocatalyst of the type TiO_2, TiO_2/M + S-SWCNT, TiO_2/M-SWCNT, and TiO_2/S-SWCNT, when the concentration of carbon nanotubes in all samples was equal to 1 wt.%.

All UV-VIS spectra shown in Fig. 5 highlight, before exposure to the light emitted by a halogen lamp, a band with a maximum at 526 nm that is assigned to the $\pi \rightarrow \pi^*$ electronic transition of Rh6G.[35] According to Fig. 5, exposure to the light emitted by a halogen lamp in the four cases induces a gradual decrease in the absorbance of the band situated in the spectral range 400–600 nm, so that after 480 min of exposure to the light emitted by a halogen lamp, the band maximum is found at 524 nm in the case of TiO_2 nanoparticles, at 520 nm in the case of TiO_2/M + S-SWCNT and TiO_2/M-SWCNT photocatalysts and 518 nm in the case of the TiO_2/S-SWCNT photocatalyst. The efficiency of photo-degradation of Rh6G in the presence of TiO_2, TiO_2/M + S-SWCNT, TiO_2/M-SWCNT, and TiO_2/S-SWCNT is equal to 31.8%, 65.4%, 66.8%, and 85.05%, respectively. These Rh6G photodegradation efficiency values are significantly higher than the value obtained in the absence of photocatalysts. The Rh6G solution alone shows only 7.8% degradation efficiency, as illustrated in Fig. S4. This result clearly indicates that the best performance in the photodegradation of Rh6G solution is achieved by the TiO_2/S-SWCNT type photocatalyst. The similar photocatalytic activity of TiO_2/M-SWCNT and TiO_2/M + S-SWCNT at 1 wt.% CNT loading indicates that, at low CNT concentrations, the

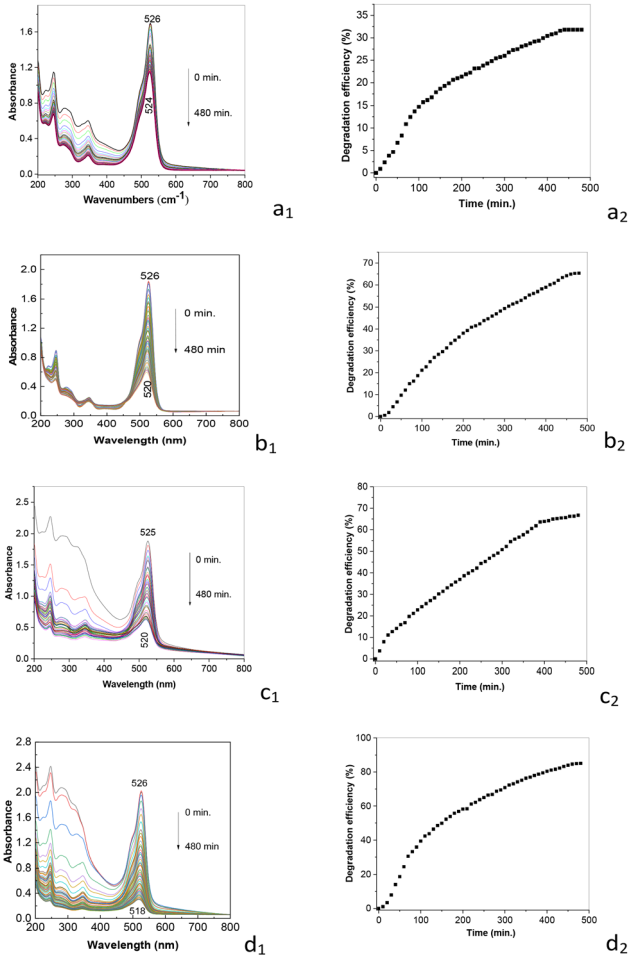

Fig. 5 Evolution of UV-VIS spectra and degradation efficiency of TiO_2 nanoparticles (a_1, a_2) and the composites TiO_2/M + S-SWCNT (b_1, b_2), TiO_2/M-SWCNT (c_1, c_2), and TiO_2/S-SWCNT (d_1, d_2) dispersed in 0.1 mM Rh6G during exposure to the light emitted by a halogen lamp for 480 min. The concentration of photocatalysts in the aqueous solution of 0.1 mM Rh6G was 0.2 mg mL^{-1}, and the concentration of carbon nanotubes in the photocatalyst mass was equal to 1 wt.%. The pH of the solution is 10.

dominant effect is the creation of conductive channels that extract electrons from TiO_2 and reduce recombination. Both M-SWCNT and M + S-SWCNT networks are sufficiently conductive to provide this function. Although the M + S-SWCNT composite contains 66% semiconducting tubes, this fraction is below the percolation threshold required for efficient visible-light sensitization and enhanced charge separation. As a result, the semiconducting tubes do not significantly influence the photocatalytic activity at this loading. In contrast, the TiO_2/S-SWCNT composite, containing 99% semiconducting tubes, provides continuous sensitization pathways and efficient electron injection, which explains its superior photocatalytic performance.

According to Fig. 6, the decrease in the apparent degradation rate at longer irradiation times is related to the fact that the TiO_2/S-SWCNT composite (1 wt.%) reaches a photodegradation efficiency of ~99% after approximately 810 min. At

such low dye concentrations, the process becomes diffusion-limited rather than photocatalysis-limited, which naturally reduces the apparent reaction rate, even though the photocatalyst remains active. The TiO_2/M-SWCNT and TiO_2/M + S-SWCNT composites exhibit similar photocatalytic activity at 1 wt.% CNT loading. Although M + S-SWCNT induces stronger interfacial tension and defect formation, both types of CNTs provide efficient electron transport pathways that reduce electron–hole recombination. At this low CNT concentration, charge carrier extraction dominates the photocatalytic behavior, leading to comparable degradation efficiencies for the two composites.

Fig. 7 clearly highlights that the TiO_2/S-SWCNT photocatalyst concentration of 0.2 mg mL^{-1} is the one that provides the best performance in the photodegradation of the 0.1 mM Rh6G solution. The result can be explained by the fact that light absorption is maximum, electron–hole recombination is minimal, and last but not least, photocatalyst agglomeration and shielding processes are minimal.

Fig. 8 highlights the influence of S-SWCNT concentration in the bulk of the TiO_2/S-SWCNT photocatalyst when a 0.2 mg mL^{-1} photocatalyst dispersion is used for the photodegradation of 0.1 mM Rh6G aqueous solution. Careful analysis of Fig. 8 highlights that during exposure to the light emitted by a halogen lamp for 480 min of the aqueous solution of Rh6G in the presence of TiO_2/S-SWCNT photocatalysts with S-SWCNT concentrations equal to 5 wt.% and 10 wt.%, a gradual decrease of the band with the maximum at 526 nm occurs until the absorption band disappears, the photodegradation efficiency of Rh6G being equal to 90.7% and 92%, respectively. The increase in the photodegradation efficiency of Rh6G, when the CNT concentration is 10 wt.% in the mass of the TiO_2/S-SWCNT photocatalyst, can be explained by the fact that the S-SWCNTs facilitate the rapid transfer of photogenerated electrons from the conduction band of TiO_2, diminishing recombination of electron–hole pairs, the resulted conductive network will allowed the adsorption of Rh6G through π–π interactions, without causing excessive UV radiation shielding or blocking of TiO_2 active sites.

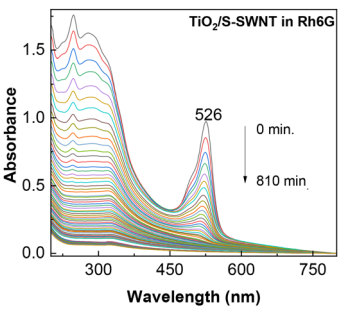

Fig. 6 Evolution of UV-VIS spectra of the TiO_2/S-SWCNT composite with a concentration of carbon nanotubes in the photocatalyst mass equal to 1 wt.%, dispersed in 0.1 mM Rh6G during exposure to light emitted by a halogen lamp, time of 810 min, when the concentration of photocatalysts in the aqueous solution of 0.1 mM Rh6G. The concentration of the TiO_2/S-SWCNT composite was 0.2 mg mL^{-1}.

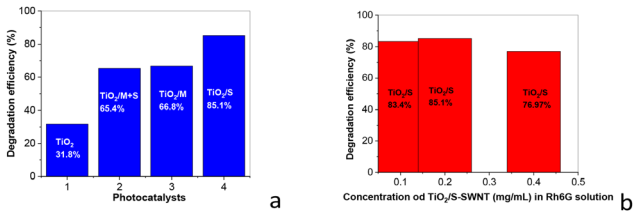

Fig. 7 Photodegradation efficiency of the 0.1 mM Rh6G aqueous solution in the presence of: (a) 0.2 mg mL^{-1} photocatalyst of the type TiO_2, TiO_2/M + S-SWCNT, TiO_2/M-SWCNT and TiO_2/S-SWCNT, having the concentration of CNTs of 1 wt% in photocatalyst mass; and (b) 0.1 mg mL^{-1}, 0.2 mg mL^{-1} and 0.4 mg mL^{-1} TiO_2/S-SWCNT, having the concentration of CNTs of 1 wt.% in photocatalyst mass.

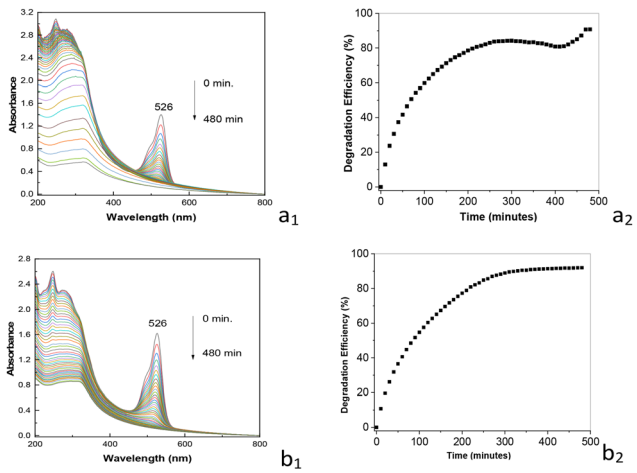

Fig. 8 The evolution of the UV-VIS spectra and degradation efficiency of the composites TiO_2/S-SWCNT, having S-SWCNT in the photocatalyst mass equal to 5 wt.% (a_1, a_2) and 10 wt.% (b_1, b_2), dispersed in 0.1 mM Rh6G during the exposure to the light emitted by a halogen lamp for 480 min. The concentration of the TiO_2/S-SWCNT dispersed in the Rh6G aqueous solution was 0.2 mg mL^{-1}.

Four steps can be invoked in the case of the photodegradation mechanism of Rh6G in the presence of catalysts: (i) adsorption of dyes; (ii) formation of photodegradation intermediate compounds; (iii) formation of final photodegradation products, and (iv) saturation of the photocatalyst surface. Thus, in the first step, Rh6G was adsorbed onto TiO_2 and the TiO_2/S-SWCNT photocatalyst's surface, with a rate constant k_1, while in the second step, the intermediate compounds resulted from the exposure of the Rh6G adsorbed onto the photocatalyst's surface, with the rate constant k_2. In the third step, the generation of the final photodegradation products occurs with a constant rate k_3, while in the fourth step, the saturation of the photocatalyst surface takes place with a constant rate k_4. Using the representation $\ln(A_0/A_t)$ as a function of time (Fig. 9), the reaction rate constants of the four steps (k_1, k_2, k_3, and k_4) for each photocatalyst, as well as the linear regression coefficients (R_1^2, R_2^2, R_3^2, and R_4^2) are calculated and pre-

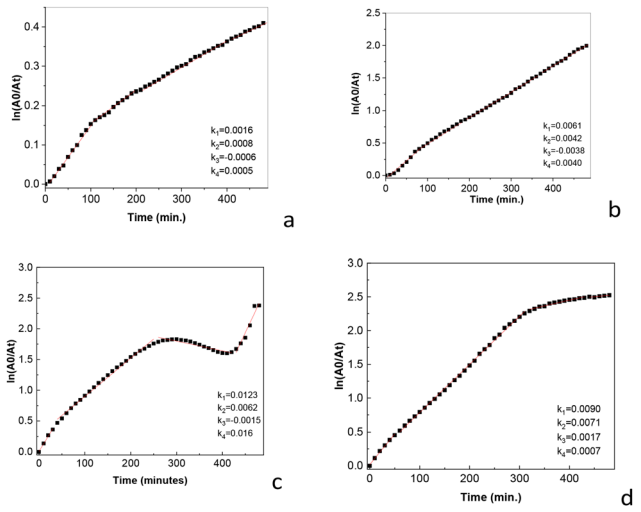

Fig. 9 Reaction kinetics of the Rh6G solution photodegradation in the presence of the photocatalysts of the type TiO_2 (a) and the TiO_2/S-SWCNT composites, having a concentration of S-SWCNT equal to 1 wt.% (b), 5 wt.% (c) and 10 wt.% (d).

sented in Table 1. Figs. 9a, b and d indicate that Rh6G photodegradation takes place according to pseudo-first-order kinetics. The presence of S-SWCNTs in the TiO_2/S-SWCNT photocatalysts mass induces an increase in the rate constants in comparison with TiO_2, as a consequence of the loading of S-SWCNTs onto TiO_2 particles. The values of the linear regression coefficients vary from 0.9011 to 0.9981. The kinetic profile of the TiO_2/S-SWCNT composite (Fig. 9c) does not follow a single pseudo-first-order trend but instead exhibits several linear regions with different slopes. This multi-stage behavior arises from the transition between distinct kinetic regimes during the photodegradation process. At early irradiation times, S-SWCNTs act as visible-light photosensitizers, enabling rapid electron injection into TiO_2 and efficient ROS formation, which results in a high apparent rate constant. As the Rh6G concentration decreases, the reaction becomes progressively limited by the diffusion of the remaining dye molecules to the catalyst surface, leading to a reduction in the apparent rate constant. The combination of sensitization-driven fast kinetics at the beginning and diffusion-limited kinetics at low dye concentration produces the characteristic curvature observed in the $\ln(A_0/A_t)$ plot.

The kinetic constants in Table 1 reveal that the TiO_2/S-SWCNT composites do not follow a single pseudo-first-order behavior but instead exhibit four distinct kinetic regimes. The 5 wt.% S-SWCNT composite shows the highest k_1 and k_4 values, indicating the most efficient initial degradation and the fastest removal of residual dye. This suggests that 5 wt.% provides an optimal balance between visible-light sensitization, charge separation, and surface adsorption. In contrast, the 10 wt.% composite exhibits the highest k_2 and k_3 values, corresponding to the degradation of intermediate species. The increased S-SWCNT content enhances visible-light absorption and electron-transfer processes, accelerating the transformation of intermediates. At this higher loading, partial shading of TiO_2 and increased light scattering may reduce the efficiency of the earliest and latest stages of the reaction, explaining why k_1 and k_4 are not maximized at 10 wt.%. These results confirm that different stages of the photodegradation process are governed by different rate-limiting mechanisms and that the optimal S-SWCNT concentration depends on the kinetic regime considered. The fastest Rh6G photodegradation is reported to be in the case of the photocatalyst TiO_2/S-SWCNT, having the concentration of CNTs in the photocatalyst mass of 5 wt.%. At S-SWCNT concentrations higher than 5 wt.% in the TiO_2/S-SWCNT composite, the excess CNTs partially shield the TiO_2 surface from the incident halogen light, reducing the effective photon flux reaching the semiconductor. This screening effect limits the visible-light sensitization efficiency of the S-SWCNTs and decreases the number of charge carriers available for interfacial redox reactions. As a consequence, the formation of reactive oxygen species such as $O_2^{\bullet-}$ and $^{\bullet}OH$ becomes less efficient, leading to a lower overall photodegradation rate of Rh6G at higher CNT loadings. To prove the significance of the $O_2^{\bullet-}$ and $^{\bullet}OH$ species, Fig. 10 shows the Rh6G photodegradation in the presence of the TiO_2/S-SWCNT composite, having a concentration of S-SWCNT in the composite mass of 1 wt.%, and scavengers of the type p-benzoquinone (BQ) and *tert*-butyl alcohol (TBA), respectively. In contrast with Fig. 5d$_1$, Fig. 10 shows a smaller decrease in absorbance of the band situated in the spectral range 400–600 nm, the photodegradation efficiency of 0.1 mM Rh6G in the presence of 0.2 mg mL^{-1} TiO_2/S-SWCNT composite, and scavengers of the type BQ (0.5 mg mL^{-1}) and TBA (1 mL) being equal to 42.55% and 18.79%, respectively. These values of the photodegradation efficiency of Rh6G indicate clearly that $O_2^{\bullet-}$ and $^{\bullet}OH$ species have a significant role in the removal process of Rh6G.

At this stage of our studies, it should be mentioned that the pH of the Rh6G solution used in the studies presented above was equal to 7.1. The influence of the pH of the Rh6G solution

Table 1 Constants of reaction kinetics of the Rh6B solution in the presence of TiO_2 and the TiO_2/S-SWCNT composites, having a concentration of S-SWCNT equal to 1 wt.% (b), 5 wt.% (c) and 10 wt.%

Photo-catalyst	k_1 (min^{-1})	R_1^2	k_2 (min^{-1})	R_2^2	k_3 (min^{-1})	R_3^2	k_4 (min^{-1})	R_4^2
TiO_2	0.0016	0.995	0.0008	0.997	0.0006	0.998	0.0005	0.997
TiO_2/S-SWCNT 1 wt.%	0.0061	0.992	0.0042	0.998	0.0038	0.998	0.0040	0.998
TiO_2/S-SWCNT 5 wt.%	0.0123	0.996	0.0062	0.998	0.0015	0.952	0.016	0.94
TiO_2/S-SWCNT 10 wt.%	0.0090	0.996	0.0071	0.999	0.0017	0.986	0.0007	0.901

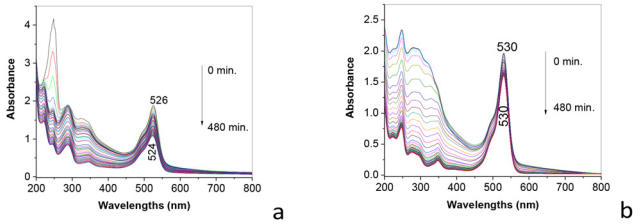

Fig. 10 Evolution of UV-VIS spectra during photodegradation of 0.1 mM Rh6G solution in the presence of 0.5 mg mL^{-1} BQ (a) and 1 mL TBA (b), and 0.2 mg mL^{-1} TiO_2/S-SWCNT composite, having the S-SWCNT concentration equal to 1 wt.%, during the exposure to the light emitted by a halogen lamp for 480 min.

on the efficiency of the TiO_2/S-SWCNT photocatalyst is illustrated in Fig. 11. In this order, 0.1 mM Rh6G solutions with pH equal to 1, 2, 4, 9, 11, and 13 were prepared by adding HCl or NaOH, the pH check being carried out with an electronic pH-meter.

According to Fig. 11, the photodegradation efficiencies of 0.1 mM Rh6G solutions with pH equal to 1, 2, 4, 9, 11, and 13, in the presence of 0.2 mg mL^{-1} of photocatalyst TiO_2/S-SWCNT, having a concentration of S-SWCNT equal to 1 wt%, were ~94%, 86.5%, 90.52%, 93.5%, 81.72%, and 78.28%, respectively. These results indicate that the photodegradation efficiency of Rh6G shows a non-linear dependence on pH. The photodegradation efficiencies greater than 90% of the TiO_2/S-SWCNT photocatalyst dispersed in 0.1 mM (0.2 mg mL^{-1}) Rh6G solutions are obtained in the case of pollutant solutions with pH equal to 1, 4, and 9. The explanation for these three pH values must take into account the fact that Rh6G is a cationic dye, which can form different species depending on the pH.[36] At pH = 1, the dye is fully protonated and reacts efficiently with photogenerated holes, while electron extraction by S-SWCNTs reduces recombination, resulting in high degradation (~94%). At pH = 4, Rh6G is stable as a monomer, which adsorbs optimally on the TiO_2/S-SWCNT surface, enabling efficient formation of both $^{\bullet}OH$ and $O_2^{\bullet-}$ species (~90.5%). At pH 2, Rh6G forms aggregated species with lower surface affinity, reducing the effective interaction with reactive species and leading to a lower degradation efficiency (~86.5%). Under basic conditions, the high OH^- concentration promotes $^{\bullet}OH$ formation. The maximum degradation at pH 9 (~93.5%) reflects an optimal balance between radical generation and dye adsorption. At pH 11 and 13, the degradation decreases (~81.7% and ~78.3%) due to reduced adsorption of the deprotonated dye and increased electrostatic repulsion between negatively charged TiO_2 and Rh6G, which limits the interaction with reactive oxygen species.

Fig. 12 shows the dependence of photodegradation efficiency of the TiO_2/S-SWCNT photocatalyst as a function of the Rh6G concentration and the number of photodegradation cycles. As expected, increasing the Rh6G concentration from 0.1 to 0.3 mM leads to a slight decrease in the pollutant photodegradation efficiency from 85.1% to 83.8% (Fig. 12a) in the presence of 0.2 mg mL^{-1} of TiO_2/S-SWCNT photocatalyst having an S-SWCNT concentration in the photocatalyst mass of 1 wt.%. Although the experiments were reproduced twice and showed consistent behaviour, this decrease should be regarded as a qualitative trend rather than a statistically significant difference. The decrease in the efficiency of Rh6G photodegradation at higher dye concentrations is consistent with the expected light-shielding effect, partial saturation of the active sites of the TiO_2/S-SWCNT photocatalyst, and the possible formation of dye aggregates, all of which reduce the availability of reactive species.

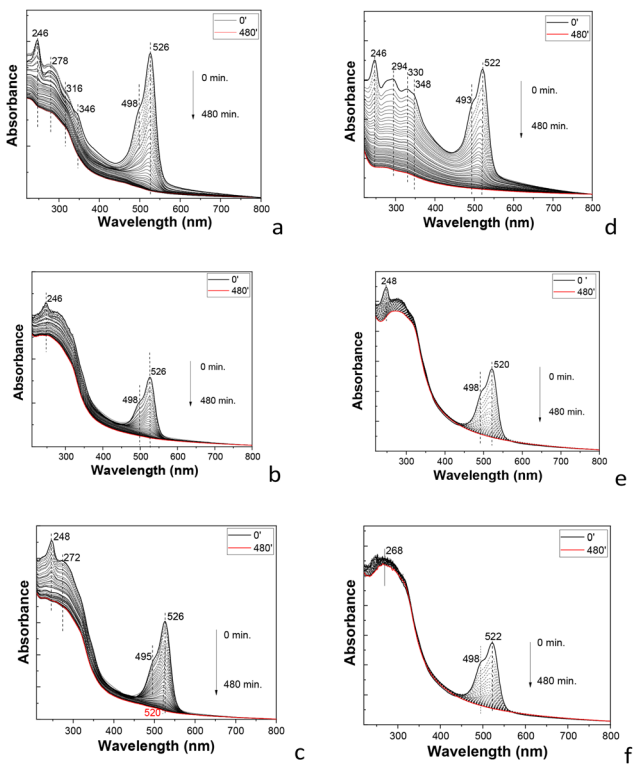

Fig. 11 UV-VIS spectra during the photodegradation of Rh6G solutions with pH = 1 (a), 2 (b), 4 (c), 9 (d), 11 (e), and 13 (f) when 0.2 mg mL^{-1} of photocatalyst TiO_2/S-SWCNT, having a concentration of S-SWNT equal to 1 wt.%, was exposed to the light emitted by a halogen lamp for 480 min.

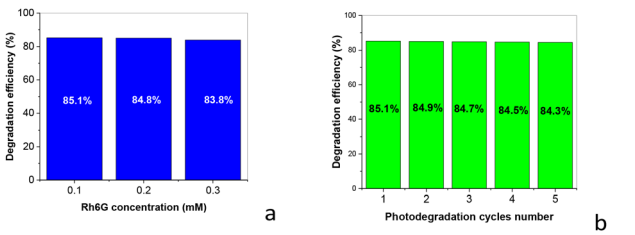

Fig. 12 Dependence of the photodegradation efficiency of the Rh6G solution in the presence of the TiO_2/S-SWCNT photocatalyst, with the S-SWCNT concentration in the composite mass of 1 wt.%, as a function of: (a) the concentration of the Rh6G solution and (b) the number of photodegradation cycles of the 0.05 mM Rh6G solution.

Although the highest Rh6G photodegradation efficiency was obtained for the composite containing 10 wt.% S-SWCNTs, the reuse tests were performed using the 1 wt.% sample. This composition was selected as a representative formulation that could be prepared in sufficient quantity to allow multiple photocatalytic cycles under identical conditions, enabling a reliable assessment of the stability of the TiO_2/S-SWCNT system.

Increasing the number of photodegradation cycles of the 0.1 mM Rh6G solution, in the presence of the 0.2 mg mL^{-1} TiO_2/S-SWCNT photocatalyst, with a S-SWCNT concentration in the photocatalyst mass of 1 wt.% by weight, leads, according to Fig. 12b, to a progressive decrease in the photodegradation efficiency of the pollutant; thus, after 5 photodegradation cycles, the efficiency reaches 84.3%. The increase in successive cycles of use of the TiO_2/S-SWCNT photocatalyst is caused by the modification of the photocatalyst surface with reaction intermediates, which results in a reduction in the number of active sites as well as the efficiency of charge separation.

At the present stage of our studies, a question remains, namely, what is the mechanism by which the higher Rh6G photodegradation efficiency can be explained in the case of the TiO_2/S-SWCNT composite compared to the TiO_2/M + S-SWCNT composite. A detailed progress concerning the photodegradation mechanisms of dyes in the presence of composites based on TiO_2 and carbonaceous materials was reported by R. Leary *et al.*[37] According to ref. 37, three photodegradation mechanisms have been considered so far. The first mechanism considers that electrons generated in the conduction band of TiO_2 are transferred to the CNTs, the transfer reducing the probability of electron–hole recombination. The second mechanism considers the injection of excited electrons in the CNTs into the conduction band of TiO_2, the holes remaining in the carbon nanotubes participating in oxidation reactions. The third mechanism considers the formation of Ti–O–C type bonds that can induce electronic states in the forbidden band, facilitating the absorption of visible light. Defects in the CNTs, such as vacancies or oxygen-based functional groups, can create additional states in the band structure, contributing to the generation of charge carriers under visible illumination. The third mechanism was reported to work simultaneously with the first two, contributing to the amplification of the photodegradation process. In comparison with these three mechanisms, in our case an important role is played by the presence of metallic tubes in the TiO_2/M + S-SWCNT composite and of semiconducting tubes in the TiO_2/S-SWCNT composites. In the case of the TiO_2/M + S-SWCNT composite, metallic nanotubes can promote faster electron–hole recombination due to their high density of electronic states, which reduces the number of electrons available for O_2 reduction and limits the formation of $O_2^{\bullet-}$ and $^{\bullet}OH$ species. We emphasize that this interpretation is based on the known electronic behavior of M-SWCNTs *versus* S-SWCNTs reported in the literature and not on direct measurements of ROS generation or recombination dynamics in this work. As a consequence, the photocatalytic degradation of Rh6G remains incomplete. In contrast, the TiO_2/S-SWCNT composite contains predominantly semiconducting nanotubes (≈99%), whose energy levels are better aligned with the conduction band of TiO_2. This alignment facilitates directional electron transfer from photoexcited S-SWCNTs to TiO_2 under visible-light irradiation, enabling more efficient O_2 reduction to $O_2^{\bullet-}$ and hole-mediated oxidation pathways leading to $^{\bullet}OH$ formation. The radicals generated through these processes contribute to a more advanced degradation of Rh6G and support the improved photocatalytic stability observed over multiple cycles.

4. Conclusions

This work reports new results concerning the photodegradation of Rh6G in the presence of photocatalysts based on TiO_2 nanoparticles and S-SWCNTs, prepared by solid-state interaction of the two constituents. The main conclusions can be highlighted as follows:

(i) solid-state interaction of TiO_2 nanoparticles with CNTs of the S-SWCNT and M + S-SWCNT type at a change in the size of TiO_2 particles from 23.67 nm to 28.2 and 150 nm, according to HRTEM studies;

(ii) XRD studies have demonstrated that the solid-state interaction of TiO_2 nanoparticles with S-SWCNT and M + S-SWCNT, respectively, leads to the separation of crystallites and to locally distorted domains;

(iii) the TiO_2/S-SWCNTs and TiO_2/M + S-SWCNT composites resulting from the solid-state interaction of the two constituents induce an increase in the I_D/I_{TM} ratio simultaneously with a decrease in the I_{RBM}/I_{TM} ratio, a consequence of the presence of surface defects and charge transfer between the two constituents of these composites as well as of tensions/strains induced in TiO_2 nanoparticles by the CNTs;

(iv) a higher efficiency of the Rh6G photodegradation is obtained in the case of the TiO_2/S-SWCNTs photocatalyst, in contrast with the TiO_2/M + S-SWCNTs photocatalyst; the highest values of the Rh6G photodegradation efficiency were equal to 92% for an S-SWCNT concentration in the photocatalyst mass of 10 wt.% and 94% for a 0.1 mM Rh6G solution with a pH equal to 1.

(vi) the photodegradation mechanism of Rh6G in the presence of TiO_2/S-SWCNTs photocatalyst takes place *via* the radicals produced, which lead to a more advanced degradation of Rh6G and good stability to multiple photodegradation cycles. In the case of the TiO_2/M + S-SWCNT composite, only a partial photodegradation of Rh6G is reported.

Author contributions

Adelina Udrescu: visualization, methodology, investigation, formal analysis. Ion Smaranda: visualization, methodology, investigation, formal analysis. Radu Cercel: visualization, methodology, investigation, formal analysis. Andreea Androne:

visualization, methodology, investigation, formal analysis. Andreea Nila: visualization, methodology, investigation, formal analysis. Elena Matei: visualization, methodology, investigation, formal analysis. Ionel Mercioniu: visualization, methodology, investigation, formal analysis. Stefano Bellucci: visualization, methodology, formal analysis. Mihaela Baibarac: methodology, investigation, formal analysis, writing – original draft, writing – review & editing, validation, supervision, conceptualization.

Conflicts of interest

There are no conflicts to declare.

Data availability

Data are available under reasonable request.

Supplementary information (SI) is available. The Supplementary Information file contains Figures S1–S4, including Raman spectra, photoluminescence spectra, electrochemical impedance spectroscopy data, and control UV-VIS measurements supporting the results presented in the manuscript. See DOI: https://doi.org/10.1039/d6dt00262e.

Acknowledgements

This work was supported by a project funded by Romania's National Recovery a Resilience Plan (PNRR), component C9. Support for the private sector, research, development, and innovation I8. "Development of a program to attract highly specialized human resources from abroad in research, development, and innovation activities", entitled "Composite materials for the applications in the water management field", ID—11/26.07.2023, contract number 760270/26.03.2024.

References

1 W. D. Wang, P. Serp, P. Kalck and L. Faris, Visible Light Photodegradation of Phenol on MWNT-TiO_2 Composite Catalysts Prepared by a Modified Sol-Gel Method, *J. Mol. Catal. A: Chem.*, 2005, **235**, 194.

2 R. Leary and A. Westwood, Carbonaceous nanomaterials for the enhancement of TiO_2 photocatalysis, *Carbon*, 2011, **49**, 741–772.

3 Q. Cao, Q. Yu, D. W. Connell and G. Yu, Titania/carbon nanotube composite (TiO_2/CNT) and its application for removal or organic pollutants, *Clean Technol. Environ. Policy*, 2013, **15**, 871–880.

4 B. Gao, G. Z. Chen and G. L. Puma, Carbon nanotubes/titanium dioxide (CNT/TiO_2) nanocomposites prepared by conventional and novel surfactant wrapping sol-gel methods exhibiting enhanced photocatalytic activity, *Appl. Catal., B*, 2009, **89**, 503–509.

5 C. Y. Yen, Y. F. Lin, C. H. Hung, Y. H. Tseng, C. C. Ma, M. C. Chang and H. Shao, The effects of synthesis, procedures on the morphology and photocatalytic activity of multi-walled carbon nanotubes/TiO_2 nanocomposites, *Nanotechnology*, 2008, **19**, 045604.

6 N. Bouazza, M. Quzzine, M. A. Lillo-Rodenes, D. Eder and A. Linares-Solano, TiO_2 nanotubes and CNT-TiO_2 hybrid materials for the photocatalytic oxidation of propene at low concentration, *Appl. Catal., B*, 2009, **92**, 377–383.

7 K. Woan, G. Pyrgiotakis and W. Sigmund, Photocatalytic carbon nanotube-TiO_2 composites, *Adv. Mater.*, 2009, **21**, 2233–2239.

8 W. Zhou, K. Pan, Y. Qu, F. F. Sun, C. G. Tian, Z. Y. Ren, G. H. Tian and H. G. Fu, Photodegradation of organic contamination in wastewaters by bonding TiO_2/single-walled carbon nanotube composites with enhanced photocatalytic activity, *Chemosphere*, 2010, **81**, 555–561.

9 L. Fu, J. Yong, G. Lai, T. Tamanna, S. Notley and A. Yu, Nanocomposite containing of multilayered carbon nanotube – titania, *Mater. Manuf. Processes*, 2014, **29**, 1030–1036.

10 Y. Chen, J. Qian, N. Wang, J. Xing and L. Liu, *In situ* synthesis of CNT/TiO_2 heterojunction nanocomposite and its efficient photocatalytic degradation of Rhodamine B dye, *Inorg. Chem. Commun.*, 2020, **119**, 108071.

11 A. S. Mestre and A. P. Carvalho, Photocatalytic degradation of pharmaceuticals carbamazepine, diclofenac, and sulfamethoxazole by semiconductor and carbon materials: A review, *Molecules*, 2019, **24**, 3702.

12 M. Ahmadi, H. R. Motlagh, N. Jaafarzadeh, A. Mostoufi, R. Saeedi, G. Barzegar and S. Jorfi, Enhanced photocatalytic degradation of tetracycline and real pharmaceutical wastewater using MWCNT/TiO_2 nanocomposite, *J. Environ. Manage.*, 2017, **186**, 55–63.

13 B. Mariafrancesca, V. M. Aleksey, V. E. Aleksey, A. Dontella, N. Anna, D. D. Leonardo, I. M. Alexandr, P. N. Fiore and D. F. Giovanni, Improving the catalytic performance of TiO2 by its surface deposition on CNT buckpapers for use in the removal of wastewater pollutants, *New Carbon Mater.*, 2025, **40**, 438–455.

14 M. R. Ardani, A. L. Pang, U. Pal, M. A. S. M. Haniff, A. G. Ismail, A. A. Hamzah, W. A. Khanday and M. Ahmadipour, Ultrasonic-assisted of TiO_2-MWCNT nanocomposite with advanced photocatalytic efficiency for elimination of dye pollutions, *Diamond Relat. Mater.*, 2023, **137**, 11066.

15 Y. Yu, J. Chen, Z. M. Zhou and Y. D. Zhao, Facile synthesis of carbon nanotube-inorganic hybrid materials with improved photoactivity, *Dalton Trans.*, 2013, **42**, 15280.

16 C. Abreu-Jauregui, L. Andronic, A. Sepulveda-Escribano and J. Silvestre-Alberto, Improved photocatalytic performance of TiO_2/carbon photocatalysts: role of carbon additive, *Environ. Res.*, 2024, **251**, 118672.

17 A. K. Singh, P. K. Vishwakarma, S. K. Pankey, R. Protop, R. Giri and A. Srivastava, A comparative study of band gap engineered *in situ* and *ex situ* MWCNTs/TiO_2 hetero-

structures for their enhanced photocatalytic activity under visible light, *Inorg. Chem. Commun.*, 2023, **150**, 110540.
18 A. Aeimbhu, J. Amonkosolpan, W. Boonyaratgalin and N. Supanam, Photocatalytic degradation of organic pollutants under solar irradiation using single-walled carbon nanotube/titanium dioxide nanocomposites, *J. Colloid Interface Sci. Open*, 2025, **20**, 100157.
19 M. G. Kim, J. M. Kang, J. E. Lee, K. S. Kim, K. H. Kim, M. Chao and S. G. Lee, Effects of calcination temperature on the phase composition, photodegradation, and virucidal activities of TiO_2 nanoparticles, *ACS Omega*, 2021, **6**, 10668–10678.
20 A. Udrescu, S. Floirca, M. Chivu, I. Mercioniu, E. Matei and M. Baibarac, Rhodamine B photodegradation in aqueous solutions containing nitrogen-doped TiO_2 and carbon nanotubes composites, *Molecules*, 2021, **26**, 7237.
21 A. Jorio, M. S. Dresselhaus and G. Dresselhaus, *Carbon Nanotubes (Topics in Applied Physics)*, Springer-Verlag, Berlin, Heidelberg, 2008, p. 111.
22 M. Baibarac, I. Baltog, A. Matea, L. Mihut and S. Lefrant, Anti-Stokes Raman spectroscopy as a method to identify the metallic and semiconducting configurations of double-walled carbon nanotubes, *J. Raman Spectrosc.*, 2015, **46**, 32–38.
23 M. Baibarac, A. Matea, M. Ilie, I. Baltog and A. Magrez, Anti-Stokes Raman spectroscopy as a method to identify metallic and mixed metallic/semiconducting configurations of multi-walled, carbon nanotubes, *Anal. Methods*, 2015, **7**, 6225.
24 M. Baibarac, I. Baltog, I. Smaranda and A. Magrez, Photochemical processes developed in composite based on highly separated metallic and semiconducting SWCNTs functionalized with polydiphenylamine, *Carbon*, 2015, **81**, 426–438.
25 A. A. Green and M. C. Hersam, Ultracentrifugation of single-walled nanotubes, *Mater. Today*, 2007, **10**, 59–60.
26 S. Guan, Y. Cheng, L. Hao, H. Yoshida, C. Tarashima, T. Zhan, T. Itio, T. Qiu and Y. Lu, Oxygen vacancies induced band gap narrowing for efficient visible-light response in carbon doped TiO_2, *Sci. Rep.*, 2023, **13**, 14105.
27 P. Paunovic, A. Grozdanov, P. Makreski, I. Dimitrievska and A. Petrovski, Structural changes of TiO_2 as a result of CNTs incorporation, *Mater. Sci. Eng. Int. J.*, 2022, **6**, 31–39.
28 H. C. Choi, Y. M. Jung and S. B. Kim, Size effects in the Raman spectra of TiO_2 nanoparticles, *Vib. Spectrosc.*, 2005, **17**, 33–38.
29 R. Sait, R. Alzahrani, N. Aslam, S. Wustoi, C. Florica, A. Diaz-Gaxiola, G. Melinte, Y. Zhang, Y. Yuan, M. N. Hedhili, S. Govindarajan, A. Syed, I. Eddine-Gallouzi, S. Inal and H. Alijawhari, Electrochemical behavior and biocompatibility of TiO2@C core-shell NWs deposited by PECVD for cellular interface application, *RSC Adv.*, 2025, **15**, 34960.
30 A. Al Mayyahi, B. M. Everhart, T. B. Shrestha, T. C. Back and P. B. Amama, Enhanced charge separation in TiO2/nanocarbon hybrid photocatalysts through coupling with short carbon nanotubes, *RSC Adv.*, 2021, **11**, 11702.
31 M. Nadafan, A. S. Alattar, Z. Dehghani and R. Malekfar, Detecting compressive strain by evaluation of Raman spectroscopy of the multiwall carbon nanotubes/TiO_2 nanocomposites, *Int. J. Nano Dimens.*, 2020, **11**, 168–176.
32 P. Corio, K. C. Silva, N. A. Soares, F. Inoue and J. J. Santos, Probing the chemical interaction between different carbon allotropes oxides and titanium dioxide nanoparticles by Raman spectroscopy, *Chem. Phys. Lett.*, 2019, **723**, 96–101.
33 P. Corio, K. C. Silva, N. A. Soares, F. Inoue and J. J. Santos, Probing the chemical interaction between different carbon allotropes oxides and titanium dioxide nanoparticles by Raman spectroscopy, *Chem. Phys. Lett.*, 2019, **723**, 96–101.
34 M. Lucas and R. Joung, Raman spectroscopic study of the effect of strain on the radial breathing modes of carbon nanotubes in epoxy/SWNT composites, *Compos. Sci. Technol.*, 2004, **64**, 2297–2302.
35 S. Bakkialakshmi, P. Selvarani and S. Chenthamarai, Absorption characterization of a dye and two amines, *Arch. Appl. Sci. Res.*, 2012, **4**, 150–154.
36 U. Roche, L. E. G. Armas, W. F. Silva, M. R. Dousti, A. L. Monra, A. Novatski, N. G. C. Astrath and C. Jacinto, Reviewing the effect of aggregates in Rhodamine 6G aqueous solution on flurescence quantum efficiency, *Spectrochim. Acta, Part A*, 2024, **317**, 124409.
37 R. Leary and A. Westwood, Carbonaceous nanomaterials for the enhancement of TiO_2 photocatalysis, *Carbon*, 2011, **49**, 741–772.

